Role of R-site magnetic moment in spin-phonon coupling in the pyrochlore iridates $R_2\text{Ir}_2\text{O}_7$: Magnetic and Raman spectroscopic investigations

Arnab Kar [*] and Suja Elizabeth[†]

Department of Physics, Indian Institute of Science, Bangalore, Karnataka 560012, India

We elucidate the role of the R-site magnetic moment in structural, electrical transport, and magnetization in three pyrochlore iridates; $\text{Dy}_2\text{Ir}_2\text{O}_7$, $(\text{Dy}_{0.5}\text{Gd}_{0.5})_2\text{Ir}_2\text{O}_7$, and $\text{Gd}_2\text{Ir}_2\text{O}_7$, where Dy^{3+} has a higher magnetic moment than Gd^{3+}. We report a semiconducting to Mott insulating transition when the compound transforms from a paramagnetic to an antiferromagnetic all-in/all-out state at temperature T_N, attributed to Ir^{4+} ordering. In $\text{Dy}_2\text{Ir}_2\text{O}_7$, the temperature-dependent irreversible magnetization M_{irr} data crossed over from negative values at a low magnetic field to positive values at high field levels below the temperature T_N, indicating magnetostriction arising from the coupling of the ordered moment with the lattice. Raman spectroscopy of the T_{2g}^4 stretching and A_{1g} bending modes around T_N reveals the spin-phonon coupling in these compounds. Specifically, in $\text{Dy}_2\text{Ir}_2\text{O}_7$, the full width at half maximum (FWHM) of Raman modes remains constant near T_N, suggesting magnetostriction in addition to spin-phonon coupling. However, in $(\text{Dy}_{0.5}\text{Gd}_{0.5})_2\text{Ir}_2\text{O}_7$ and $\text{Gd}_2\text{Ir}_2\text{O}_7$, where Gd^{3+} substitutes for Dy^{3+}, no evidence of magnetostriction is observed in either magnetization or Raman data, although an increase in the FWHM of Raman modes near T_N suggests only the presence of weak spin-phonon coupling. Furthermore, the temperature-dependent lattice constant confirms the presence of magnetostriction in $\text{Dy}_2\text{Ir}_2\text{O}_7$.

I. INTRODUCTION

Geometric frustration is widely studied because it plays a vital role in many diverse phenomena in the broad field of condensed matter physics [1,2]. Geometric frustration in a system indicates that the local lattice geometry prevents minimizing the energy between pairs of neighboring interacting spins to form the classical ground state [3,4]. Pyrochlores are ideal candidates to explore the effect of frustration in three-dimensional lattices. The pyrochlore structure in compounds with the chemical composition $R_2B_2O_7$ shows unique physical behavior like spin liquid states, spin ice states, metal-insulator transitions, and superconductivity [5,6]. In pyrochlore $R_2B_2O_7$ compounds, a trivalent lanthanide may occupy the R site, and the B site may be occupied by a tetravalent transition metal where the interpenetrating corner-shared tetrahedra of R and B cations introduce geometric frustration [3]. Recently, there has been much interest in Ir-based pyrochlores ($R_2\text{Ir}_2O_7$) due to their ability to generate novel topological phases. We can attribute this to the presence of extended $5d$-based heavy Ir atoms, which facilitate the correlation between spin-orbit coupling (SOC), electron correlation U, and the crystal-field effect in the comparable energy scale [7–10].

Interestingly, pyrochlore iridates exhibit a metal-insulator transition (MIT) where the Ir^{4+} tetrahedra start to order in an all-in/all-out (AIAO) antiferromagnetic state [11–16]. But $\text{Pr}_2\text{Ir}_2O_7$ is an exception and remains in a paramagnetic metallic state after the temperature is lowered [17,18].

In the AIAO magnetic structure, spins at the four vertices of the Ir tetrahedra point inward (all in) or outward (all out) from the center of the tetrahedron. The noncollinear spin configuration and the presence of $5d$ Ir atoms give rise to strong Dzyaloshinskii-Moriya interaction, which induces spin-phonon coupling (SPC) [19]. SPC via SOC interaction has explained many phenomena like the thermal Hall effect, spin relaxation in the spintronic field, stabilization of a specific ground state with epitaxial strain, etc. [20–23]. Recent studies using Raman spectroscopy on pyrochlore iridates reported anomalies in phonon spectra below the magnetic ordering temperature T_N [24]. The authors observed an anomalous behavior of pyrochlore iridates with nonmagnetic R sites near T_N due to the spin-phonon coupling [25,26]. Likewise, if spin-coupled lattices have elastic degrees of freedom, strain accompanies the magnetic transition and results in magnetostriction in the sample [27]. These results motivated us to study lattice dynamics in pyrochlore iridates with a magnetic R site. In selecting Dy^{3+} ions for the R site, we may be able to clarify the role of magnetic ions in the electronic, magnetic, and structural properties in pyrochlore iridates. Further, by changing the strength of the magnetic moment at the R site, it is feasible to examine the tunability of SPC. A previous report demonstrated that it is possible to tune the physical properties by substituting magnetic ions for nonmagnetic ions at the R site [28]. We probed the effect of varying the R-site magnetic moment without perturbing the crystal structure. The Dy^{3+} ion has a higher magnetic moment, $\mu_{\text{exp}} = 10.63\mu_B$ (where μ_{exp} is the experimentally observed magnetic moment) [29], and is an ideal candidate to study the role of the rare-earth magnetic moment in more detail. We substituted the Dy^{3+} rare-earth ion with a Gd^{3+} ion with a lower magnetic moment ($\mu_{\text{exp}} = 7.98\mu_B$) [29] to observe the change in properties due

*arnabkar@iisc.ac.in
†liz@iisc.ac.in

to the dilution of the magnetic moment. As the ionic radii of Gd and Dy do not differ much, their structural properties are not expected to change drastically.

We synthesized and studied phase-pure samples of the pyrochlore iridates $Dy_2Ir_2O_7$, $(Dy_{0.5}Gd_{0.5})_2Ir_2O_7$, and $Gd_2Ir_2O_7$. We report the effect of Gd^{3+} substitution in the R site on the physical properties of the pyrochlore iridates. In $Dy_2Ir_2O_7$, the magnetic ordering of Ir^{4+} occurs at a temperature much higher than its MIT temperature. We further investigate the spin-lattice dynamics involved in ordering the temperature by the temperature evolution of Raman spectra. In this paper, we denote $Dy_2Ir_2O_7$, $(Dy_{0.5}Gd_{0.5})_2Ir_2O_7$, and $Gd_2Ir_2O_7$ as DIO, DGIO, and GIO, respectively.

II. EXPERIMENTAL DETAILS

We synthesized polycrystalline samples of DIO, DGIO, and GIO using the conventional solid-state method. High-purity precursors of $Dy_2O_3(3N)$, $Gd_2O_3(3N)$, and $IrO_2(3N)$ powders were first mixed in a stoichiometric ratio with 10% extra IrO_2 to combat volatility at high temperature. After mixing and grinding thoroughly, we pressed the powder mixture into a pellet and heated it at 1373 K for several days with intermediate grinding. The phase purity of these synthesized samples was checked using powder x-ray diffraction (XRD; Rigaku diffractometer with Cu $K\alpha$ radiation). XRD data collected in the 2θ range of $10°$–$90°$ in steps of $0.02°$ were refined using the Rietveld refinement software (FULL-PROF) [30]. Using the VESTA software [31], we calculated the bond lengths and the bond angles. The oxidation state of Ir ions was determined using x-ray photoelectron spectroscopy (XPS; AXIS Ultra spectrometer), and we analyzed the data with the CASAXPS spectroscopy software [32]. A four-probe method was used to measure temperature-dependent resistivity from 4 to 300 K in a closed-cycle refrigerator. The DC magnetization was probed using a magnetic property measurement system (Quantum Design) with a superconducting quantum interference device in the temperature range of $5 \leqslant T \leqslant 400$ K in both zero-field-cooled (ZFC) and field-cooled-warming (FCW) protocols. In the ZFC protocol, the sample cools without any field, and the data are obtained when the sample warms in an external magnetic field. In the second protocol (FCW), the sample cools under the same external field and then yields data on warming. There was no difference (or hysteresis) between FCW and field-cooled-cooling (FCC) data (recorded while cooling) with the same magnetic field applied. We recorded the temperature-dependent Raman spectra (Labram-HR800 micro-Raman spectrometer with 473 nm excitation source) in the temperature range of 80 to 300 K using liquid N_2. Raman spectra were fitted with Lorentzian functions to obtain the frequency and linewidth [full width at half maximum (FWHM)] of individual Raman modes. Temperature-dependent powder x-ray diffraction (PXRD) measurements were conducted on the parent samples ($Dy_2Ir_2O_7$ and $Gd_2Ir_2O_7$), utilizing a Bruker D8 Discover XRD machine with Cu $K\alpha$ radiation. The PXRD data recorded at various temperatures ranging from 70 to 300 K were refined using the FULLPROF software for Rietveld refinement [30].
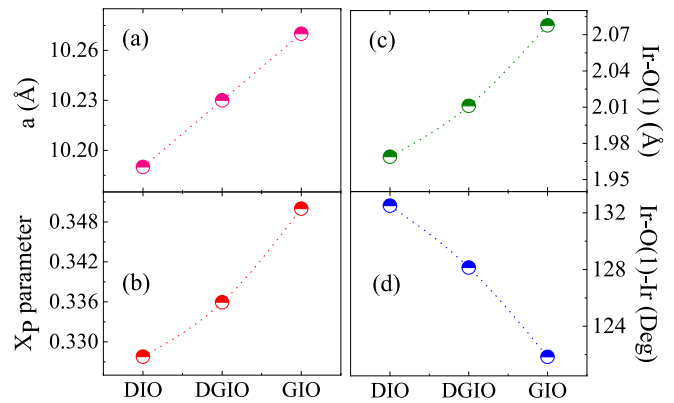

FIG. 1. (a) Lattice constant a, (b) X_P parameter [x position of the O(1) atom], (c) Ir-O(1) bond length, and (d) Ir-O(1)-Ir bond angle in DIO, DGIO, and GIO samples. Dashed lines are a guide to the eye.

III. RESULTS AND DISCUSSION

A. Structural analysis

The Rietveld refinements of room temperature XRD patterns for DIO, DGIO, and GIO (Fig. S1 in the Supplemental Material [33]) indicate that all samples crystallize in the cubic $Fd\bar{3}m$ space group. The unit-cell parameters are $a = 10.19$ Å, $a = 10.23$ Å, and $a = 10.27$ Å for DIO, DGIO, and GIO, respectively [Fig. 1(a)]. Changes in the lattice parameter are likely to result since the ionic radius of the Dy^{3+} ion (1.027 Å) is less than that of the Gd^{3+} ion (1.053 Å); when Gd^{3+} is substituted for Dy^{3+}, the lattice parameter elongates. In the pyrochlore structure, the x position of oxygen atom O(1) at the $48f$ Wyckoff position (X_P parameter) may play a major role in determining the electronic and magnetic properties like in the structural organization of $IrO(1)_6$ octahedra and their physical properties [34]. In an undistorted $IrO(1)_6$ octahedron, all six Ir-O(1) bond lengths are equal, and the corresponding X_P parameter is $X_{ideal} = 0.3125$, creating a perfect local cubic crystal field. Deviation of X_P from this X_{ideal} value introduces a trigonal crystal field, which splits the degenerate t_{2g} orbitals into singlet a_{1g} and doublet e'_g states, thus modifying the orbital ordering or local hybridization [35]. From Rietveld refinement, the X_P parameters are 0.32, 0.34, and 0.35 for DIO, DGIO, and GIO, respectively. Figure 1(b) shows the evolution of the X_P parameter with Gd^{3+} substitution. The increase in the X_P parameter due to Gd^{3+} substitution indicates the increase of the trigonal distortion in $IrO(1)_6$ octahedra. Changes in the X_P parameter caused by the Ir-O(1) bond length and $\langle$Ir-O(1)-Ir$\rangle$ bond angle are shown in Figs. 1(c) and 1(d), respectively. These plots indicate that substituting Gd^{3+} increases the Ir-O(1) bond length, while the bond angle $\langle$Ir-O(1)-Ir$\rangle$ decreases. As a result, the distortion in the $IrO(1)_6$ octahedra has a bearing on the hopping of itinerant Ir $5d$ electrons. The crucial role of the X_P parameter in our systems is consistent with that reported earlier [36].

B. X-ray photoelectron spectroscopy

To investigate the role of Ir in the electronic and magnetic properties [37], we performed XPS measurements on all three synthesized polycrystalline samples. We employed the stan-

TABLE I. Binding energy (BE) for different oxidation states of Ir ions. The percentage (%) was obtained from fitting experimental XPS data using CASAXPS software for all three samples.

Oxidation	DIO		DGIO		GIO	
state	BE (eV)	%	BE (eV)	%	BE (eV)	%
Ir^{4+} $4f_{7/2}$	61.99	93.06	62.02	82.42	61.57	83.36
Ir^{4+} $4f_{5/2}$	65.16		64.97		64.34	
Ir^{3+} $4f_{7/2}$		0	60.88	17.58	60.42	16.64
Ir^{3+} $4f_{5/2}$			63.81		63.05	
Ir^{5+} $4f_{7/2}$	64.01	6.94		0		0
Ir^{5+} $4f_{5/2}$	67.01					

dard CASAXPS software package to fit the XPS spectra (Fig. S2 in the Supplemental Material [33]). The detailed fitting shows that the Ir^{4+} ionic state makes a significant contribution. For DIO, the relative ratio of Ir^{4+}:Ir^{5+} is found to be 0.93 : 0.07. The presence of Ir^{5+} due to oxygen vacancies in the sample may modify the electronic and magnetic properties. The measurement results for DGIO and GIO are summarized in Table I. The relative ratios of Ir^{5+} (in the case of DIO) and Ir^{3+} (for the other two samples) to Ir^{4+} indicate that a similar oxidation state (species) is present in all the samples. Small changes in the peak position and FWHM values of spin-orbit peaks of Ir^{4+} are due to a modification in the Ir environment in $IrO(1)_6$ octahedra caused by the difference in oxygen vacancies [38–40].

C. Electrical transport

Figure 2 shows the temperature-dependent resistivity $\rho(T)$ of all samples after normalizing its value at 300 K, as recorded during the heating cycle from 4 to 300 K. A transition is evident in Fig. 2, where the resistivity $\rho(T)$ increases by four orders of magnitude at low temperatures in DIO and GIO and up to three orders for DGIO samples. Similar MITs are seen in DIO and GIO, as reported earlier [11,12]. Although a slope change is visible near 100 K in $\rho/\rho(300)$ vs T plots,

there is no evidence of metallic behavior above the transition. An enlarged graph near the transition region is shown in the inset in Fig. 2. The MIT temperatures T_{MIT} for DIO, DGIO, and GIO are 113, 110, and 108 K, respectively (Fig. S4 in the Supplemental Material [33]). We fitted the resistivity data using the Arrhenius equation above T_{MIT} as

$$\rho(T) = \rho_0 \exp(E/T). \qquad (1)$$

Here, ρ_0 is the temperature-independent resistivity, and E is the activation energy. Figures 3(a)–3(c) represent the fitting for DIO, DGIO, and GIO, respectively. The energy gap of all the samples is on the order of meV, a result which indicates semiconducting behavior with a small energy band gap above T_{MIT} [12]. Most pyrochlore iridates exhibit Mott insulating behavior at low temperatures [8,41,42]. We can express this using the variable-range hopping (VRH) model [43] as

$$\rho(T) = \rho_0' exp(T_0/T)^{1/4}, \qquad (2)$$

where ρ_0' is a temperature-independent resistivity coefficient and T_0 is the characteristic temperature. In general, the VRH
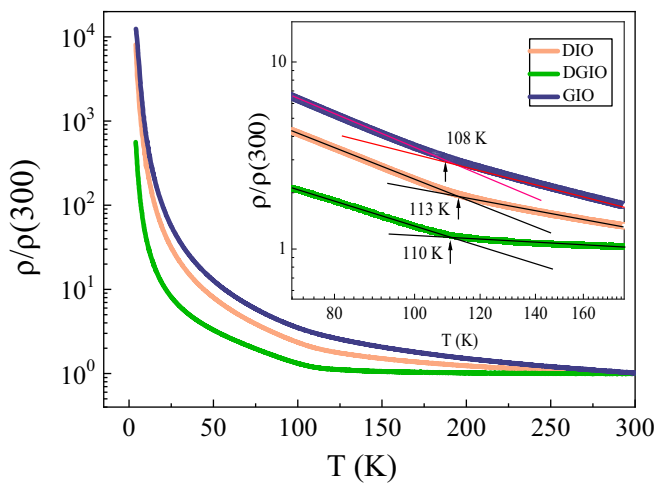

FIG. 2. Temperature-dependent resistivity data normalized to $\rho(300)$ for DIO, DGIO, and GIO. The inset shows an enlarged view near MIT, where the black and red straight lines are drawn to indicate the slope changes near T_{MIT}.
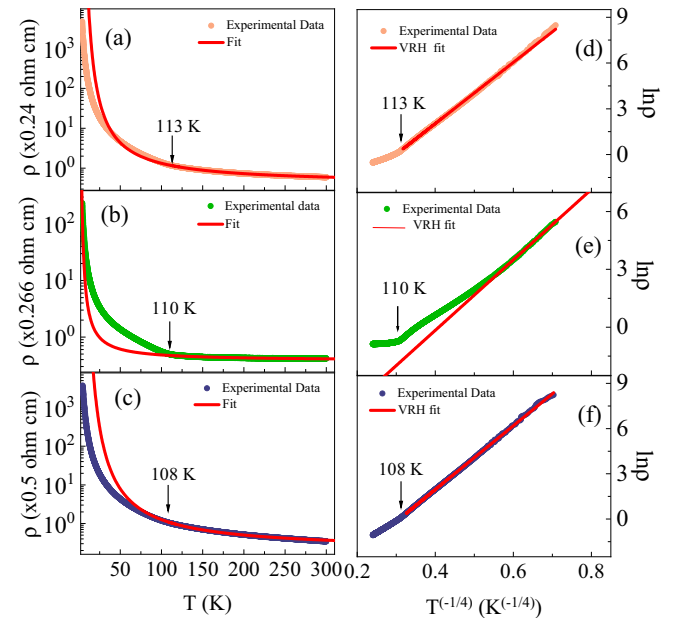

FIG. 3. $\rho(T)$ data fitted with Eq. (1) above T_{MIT}: (a) DIO, (b) DGIO, and (c) GIO. $\rho(T)$ data plotted in $\ln\rho$-$T^{-1/4}$ scale and fitted with the VRH model (2) below T_{MIT}: (d) DIO, (e) DGIO, and (f) GIO. Solid red lines denote the fitting.

TABLE II. Fit parameters ρ_0, T_0, and localization length a' calculated using Eq. (3).

Sample	ρ_0' (Ω cm)	T_0 (10^5 K)	a'(Å)
DIO	2.4×10^{-3}	1.62	5.05
DGIO	5.67×10^{-4}	1.12	5.72
GIO	1.49×10^{-3}	2.00	4.70

model is related to the localization of carriers by disorder caused by long-range Coulomb interactions [44]. The fitted resistivity data are presented in Figs. 3(d)–3(f). Below T_{MIT}, experiment data conform to the VRH model for DIO and GIO; for DGIO, a hump is seen just below the transition temperature. It indicates that DGIO does not transform directly to the Mott insulating phase and needs additional probing. We deduced the values of ρ_0' and T_0 from the best fit, and they are listed in Table II. The characteristic temperature T_0 is given by

$$T_0 = \frac{18}{k_B(a')^3 N(E_F)}. \tag{3}$$

Here, k_B is Boltzmann's constant, a' is the localization length, and $N(E_F)$ is the density of states at the Fermi level. By adopting a value of $N(E_F)$ of 10^{28} eV^{-1} m^{-3} [45] from a previous report on pyrochlore iridates, we calculated the localization length a' in the compound using Eq. (3). Its magnitude is in the angstrom range and is comparable to that of the Ir-O(1) bond length obtained from XRD analysis. It validates the VRH mechanism prevalent at low temperatures.

We note from the above study that when Gd^{3+} is substituted for Dy^{3+}, the value of T_{MIT} decreases gradually. The Ir-O(1) bond length increases, and the Ir-O(1)-Ir bond angle decreases. The resistivity of the pyrochlore iridate is known to depend on Ir^{4+} ions having unpaired electrons in the half-filled $J_{eff} = 1/2$ t_{2g} state [8,36,46]. The changes in bond lengths and angles affect the electron hopping between neighboring sites via the O 2p orbital, thus causing a change in the magnitude of the resistivity of the substituted sample. The X_P parameter has linkages to the trigonal distortion in the IrO(1)$_6$ octahedra and increases as the concentration of Gd^{3+} increases. The distortion also lifts the degeneracy of the t_{2g} states [35]. The energy gap between the split states depends on the extent of the distortion in the IrO(1)$_6$ octahedra, which causes the observed change in the transition temperature T_{MIT}. The trace oxidation elements Ir^{3+} and Ir^{5+} present in the samples influence the electrical transport properties [37,40]. Since Ir^{3+} contains filled states and Ir^{5+} has empty $J_{eff} = 1/2$ states, the electron hopping between neighboring sites is also affected.

D. Magnetization

Figure 4 illustrates the temperature evolution of magnetization $M(T)$ at 1000 Oe for all samples measured using the ZFC and FCW protocols. Magnetic irreversibility between the ZFC and FCW protocols manifests as a gap (opening) in the two plots below the temperature T_{irr}. Resonant x-ray diffraction, neutron powder diffraction, and muon spin rotation and relaxation studies revealed that Ir^{4+} moments order in an all-in/all-out antiferromagnetic structure below T_{irr} in
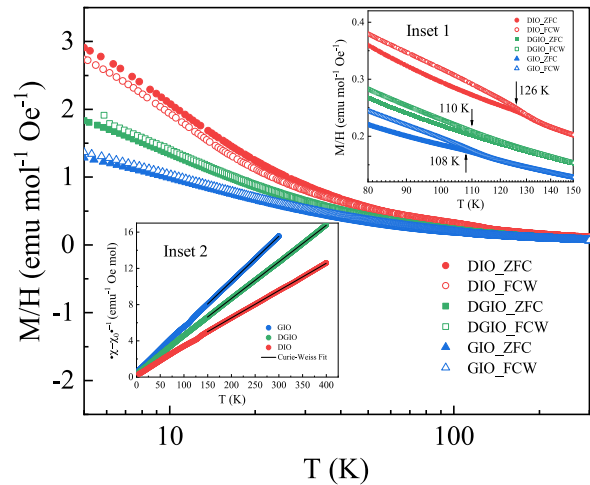

FIG. 4. Temperature-dependent ZFC-FCW data at $H = 1000$ Oe. Inset 1 shows a zoomed-in view in the region of transition temperature T_N, where all three samples show the bifurcation between ZFC and FCW data. Inset 2 presents the inverse of the modified χ with the temperature, where black solid lines are the Curie-Weiss fitting for three samples.

iridates with similar magnetic behavior [13–15,47]. Hence, T_{irr} is considered an onset of long-range antiferromagnetic ordering. Inset 1 in Fig. 4 shows the ordering temperatures $T_N = 126$, 110, and 108 K for DIO, DGIO, and GIO, respectively (Fig. S5 in the Supplemental Material [33]). As the rare-earth ordering commences due to interaction with the ordered Ir magnetic structure at low temperature, the magnetic moment of the sample reduces as the substitution of Gd^{3+} (magnetic moment is lesser than that of Dy^{3+}) progresses [48]. Cathelin et al. reported a value of T_N of 125 K for their powder DIO sample [49]. Except for DIO, we found that the magnetic ordering begins when the material undergoes MIT. The coincidence of Ir^{4+} ordering and MIT is a distinctive characteristic when the transport properties are primarily mediated by itinerant electrons of Ir ions. In the case of DIO, the higher magnetic moment of Dy^{3+} will force the magnetic transition to occur at a higher temperature and decouple the two transitions. The decoupling of T_{MIT} and T_N was the subject of an earlier study [50].

At high temperature (150–400 K), the samples are in a paramagnetic state. Magnetic susceptibility $\chi = M/H$ was analyzed using a modified Curie-Weiss law,

$$\chi = \chi_0 + \frac{C}{T - \theta_P}, \tag{4}$$

where χ_0, C, and θ_P are the temperature-independent magnetic susceptibility, Curie constant, and Curie-Weiss temperature, respectively. In DIO, the fitted data yield $\chi_0 = 2.5 \times 10^{-3}$ emu/mole, $C = 33.15$ K, and $\theta_P = -16.5$ K. We calculated the effective paramagnetic moment μ_{eff} using the value of the Curie constant C and the frustration parameter f' using the ratio $|\theta_P|/T_N$ for all three samples. The results are given in Table III. Inset 2 in Fig. 4 gives the modified inverse susceptibility $(\chi - \chi_0)^{-1}$ vs T. It shows linear behavior and fits well with Eq. (4) (solid black lines represent fit data). The frustration parameter signifies the magnetic frustration

TABLE III. Parameters obtained by fitting M-T data with the modified Curie-Weiss equation (4) at high temperatures.

Sample	χ_0 (emu mol^{-1} Oe^{-1})	θ_P (K)	C (K)	$f = |\theta_P|/T_N$	μ_{eff}[exp] (μ_B/f.u.)	μ_{eff}[cal] (μ_B/f.u.)
DIO	2.5×10^{-3}	-16.5	33.15	0.134	16.28	15.24
DGIO	1.41×10^{-3}	-14.24	24.716	0.129	14.05	13.45
GIO	3.77×10^{-3}	-12.22	20.085	0.113	12.67	11.45

in the sample. For $f = 1$, ordering commences according to its exchange-interaction strength, whereas the systems with much higher f values (> 10) are frustrated systems. For our samples, the value of f is very low (< 1), which indicates a small magnitude of $|\theta_P|$ compared to the magnetic transition temperature T_N. This is due to the high f-d interaction between localized rare-earth $4f$ and itinerant Ir $5d$ electrons. In Table III, we can see that the value of the f parameter decreases with increasing levels of Gd^{3+} substitution. The reason is that the f-d exchange interaction reduces with an increase in dilution magnetic moment in the R site [36,51].

In Table III, we tabulate the values of μ_{eff}[exp] obtained from the Curie constant C and μ_{eff}[cal] calculated using the following equation for all three samples:

$$\mu_{\mathrm{eff}}[\mathrm{cal}] = \sqrt{x_1(\mu_{Dy^{3+}})^2 + x_2(\mu_{Gd^{3+}})^2 + y(\mu_{Ir^{4+}})^2}, \quad (5)$$

where x_1, x_2, and y are the compositions of the Dy^{3+}, Gd^{3+}, and Ir^{4+} ions, respectively, in the samples. The percentage of Ir^{4+} ions was estimated from the XPS study. We used the rare-earth effective moment from Ref. [29], calculated the effective magnetic moment Ir^{4+} ions, and obtained μ_{eff}[cal] for all three samples. Ir^{3+} and Ir^{5+} ions are not considered in the calculation because they are nonmagnetic ions. It is noticeable from Table III that the experimental values are in good agreement with the expected values.

We noticed an anomaly in ZFC and FCW data for the DIO sample. So we further investigated the difference between FCW and ZFC. Temperature evolutions of $M_{\mathrm{irr}} = M_{\mathrm{FCW}} - M_{\mathrm{ZFC}}$ for DIO, DGIO, and GIO are shown in Fig. 5(a) under magnetic field $\mu_0 H = 0.1$ T. As expected, M_{irr} has zero value in the paramagnetic region. Below the magnetic transition temperature T_N, M_{irr} increases to a finite value. In Fig. 5(a), we see a reversal in the slope of the graph near 100 K for DIO. Here, ZFC starts to dominate over FCW, yielding negative values of M_{irr} at low temperatures, whereas in the case of DGIO and GIO, M_{irr} remains positive up to the lowest measured temperature. The unusual behavior of $M_{\mathrm{irr}}(T)$ for the DIO sample with ZFC and FCW data crossing over indicates the presence of magnetostriction in the material [52]. Magnetostriction originates when the magnetic moments of atoms are coupled with the elastic degrees of the lattice in the sample. Below T_N, ordered AIAO Ir^{4+} tetrahedra apply an internal field H_{loc} on Dy^{3+} tetrahedra through f-d exchange interaction. Strong f-d exchange interaction in DIO tries to order Dy^{3+} tetrahedra, which couple with the lattice and generate magnetostriction in the sample. Figures S6(a) and S6(b) in the Supplemental Material [33] show the ZFC and FCW data for the DIO sample in the presence of lower magnetic fields ($\mu_0 H = 0.01, 0.05$ T). The plots show that lowering the applied external field increases the difference

between FCW and ZFC at low temperature. The magnetostriction effect increases with decreasing applied field. External magnetic field opposes ordering of Dy^{3+} tetrahedra, which, in turn, reduces internal field, leading to magnetostriction. This is evident in the variation of M_{irr} with external field shown in Figs. 5(b). However, as the field increases beyond a threshold value ($\mu_0 H = 1$ T), magnetostriction is suppressed, resulting in positive values of M_{irr} [Fig. 5(b)]. The reduced f-d exchange interaction strength that results from lowering the R-site magnetic moment is reflected in the temperature dependence M_{irr} data for the DGIO and GIO compounds, in which the positive values occur throughout the temperature range. This shows that the low R-site moment due to Gd^{3+} substitution is not sufficient to invoke magnetostriction in Gd-based iridates [53].

E. Raman spectroscopy

We recorded temperature-dependent Raman spectra of three samples to understand the variations in phonon spectra and verify the spin-phonon and spin-lattice coupling (magnetostriction) as discerned from the magnetic irreversible data. Group theoretical analysis predicted six Raman active modes
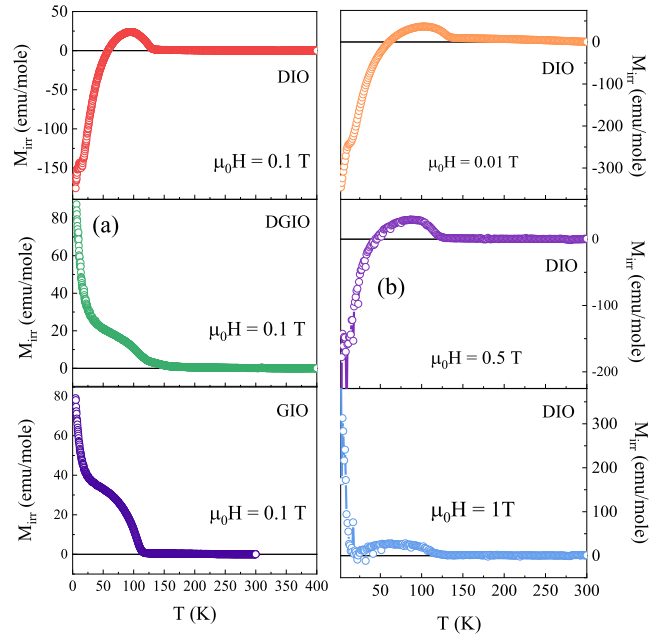

FIG. 5. (a) Temperature dependence of the irreversible magnetization $M_{\mathrm{irr}} = M_{\mathrm{FCW}} - M_{\mathrm{ZFC}}$ for DIO, DGIO, and GIO at external field $\mu_0 H = 0.1$ T. (b) Temperature dependence of the irreversible magnetization M_{irr} in DIO at different external fields, $\mu_0 H = 0.01$, 0.5, and 1 T.
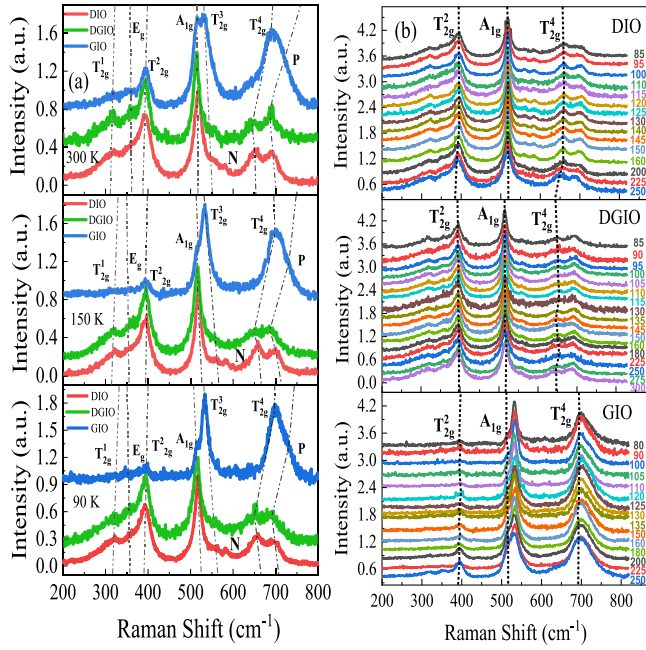
FIG. 6. (a) Raman spectra measured at 300 K (top), 150 K (middle), and 90 K (bottom) for DIO, DGIO, and GIO. (b) Raman spectra recorded at different temperatures for DIO (top), DGIO (middle), and GIO (bottom). Data are shifted vertically for better visualization.

($\Gamma^R = A_{1g} + E_g + 4T_{2g}$) for this family ($Fd\bar{3}m$ space group), a general consequence of the movement of the oxygen atoms [54–56]. Figure 6(a) represents Raman modes for all three samples at 300, 150, and 90 K. We observe all six modes in all compounds at values of 320, 355, 392, 515, 556, and 650 cm^{-1}, which are assigned to the T_{2g}^1, E_g, T_{2g}^2, A_{1g}, T_{2g}^3, and T_{2g}^4 Raman modes, respectively [54]. In addition, Raman spectra show two extra peaks at 582 and 700 cm^{-1}, which we denote as N and P modes, respectively. The N mode is prominent for the DIO sample. P is often called the second-order Raman scattering mode for pyrochlore oxides [57]. Slight changes are observed in a few Raman peaks due to changes in the lattice parameters because of the Gd^{3+} substitution. To distinguish T_{2g}^4 and P modes for the GIO sample, we deconvoluted the broad peaks near 700 cm^{-1} by fitting two Lorentzian peaks (Fig. S7 in the Supplemental Material [33]). These results agree with previous reports on pyrochlore iridates [25,26]. Temperature-dependent Raman studies provide more insights into the evolution of structural symmetry with temperature in these samples. Figure 6(b) shows the Raman spectra recorded at different temperatures for DIO, DGIO, and GIO. It does not show a change in the peak position or appearance (or disappearance) of any peak as the temperature decreases. We conclude that there is no structural phase change in these samples in the measured temperature range, which is consistent with previous reports [26,47].

Raman modes result from the movement of the oxygen atoms in Ir-O(1), R-O(1), and R-O(2) stretching and Ir-O(1)-Ir bending vibrations. O(1) and O(2) denote the oxygen atoms at the 48f and 8b sites, respectively. In the observed spectra, the most intense peaks are T_{2g}^2, A_{1g}, and T_{2g}^4. R-O(1) stretching

dominated the low-frequency T_{2g}^2 mode, the high-frequency T_{2g}^4 mode involves Ir-O(1) stretching, and the A_{1g} mode is due to Ir-O(1)-Ir bending [24]. We recall that the X_P parameter is related to the trigonal distortion in the pyrochlore system discussed earlier in Sec. III A. The trigonal distortion is affected by the Ir-O(1) bond length and Ir-O(1)-Ir bond angle and, in turn, modifies the T_{2g}^4 and A_{1g} Raman active modes [55]. We investigate, in detail, these two Raman modes (A_{1g}, T_{2g}^4) with a view to understanding the effects of temperature and Gd^{3+} substitution on magnetic ordering.

The temperature dependence of the phonon frequencies of Raman modes T_{2g}^4 and A_{1g} are shown in Figs. 7(a)–7(c) for all three samples near T_N. We observe anomalies near the magnetic transition in the plots for DIO and DGIO, whereas the anomalies are not prominent in GIO. We also explore the influence of temperature on the frequency of the A_{1g} and T_{2g}^4 modes. Ir(5d)-O(2p) hybridization has a significant role in the T_{2g}^4 mode which is mainly due to the stretching vibration of Ir-O(1) [56,58]. The decrease in temperature affects the Ir-O(1) bond length [26] in addition to changes near the magnetic ordering temperature [59]. Thus, one would expect corresponding changes in the T_{2g}^4 Raman mode, which we see in our data. The substitution of the Gd^{3+} ion lowers the f-d exchange interaction and hence the coupling strength with the lattice. It explains why the anomaly becomes less prominent near T_N in GIO. In the A_{1g} mode, the anomalous behavior near the magnetic ordering temperature may be due to a sudden rotation/distortion of IrO(1)$_6$ octahedra. The reason is that the A_{1g} mode mediates through the Ir-O(1)-Ir bending vibration and is directly related to the oxygen X_P parameter of IrO(1)$_6$ octahedra. Others reported a similar observation in the XRD analysis and temperature dependence study of the X_P parameter [60].

The origin of Raman modes is attributable to various factors, such as phonons, magnons, spin-phonon coupling, magnetostriction, etc. [26,27,61]. So the temperature dependence of the phonon frequency can be written as $\omega(T) = \omega_{\text{anh}}(T) + \Delta\omega_{\text{el-ph}}(T) + \Delta\omega_{\text{sp-ph}}(T)$. $\omega_{\text{anh}}(T)$ is the anharmonic contribution when there is no coupling of phonons. The Balkanski anharmonic decay model [62] expresses the temperature dependence of the frequency of the modes as

$$\omega_{\text{anh}}(T) = \omega_0 - C\left[1 + \frac{2}{(e^{\hbar\omega/2k_BT} - 1)}\right]. \quad (6)$$

Here, C and ω_0 are fitting parameters, $\hbar\omega$ is the phonon energy, and k_B is the Boltzmann constant. The Raman modes and fitting of Eq. (6) for all samples are shown in the Supplemental Material (Fig. S8) [33]. A deviation from the anharmonic dependence of the phonon frequency near T_N can be seen (except in the GIO T_{2g}^4 mode). This deviation from the $\omega_{\text{anh}}(T)$ term indicates the presence of $\Delta\omega_{\text{el-ph}}(T) + \Delta\omega_{\text{sp-ph}}(T)$ terms in our samples. $\Delta\omega_{\text{el-ph}}(T)$ denotes the change in phonon frequency due to electron-phonon coupling. As our compounds transform into a Mott insulating phase below T_N, we can neglect this electron-phonon coupling term. So the deviation near the magnetic transition temperature suggests a spin-phonon coupling term $\Delta\omega_{\text{sp-ph}}(T)$. In the model proposed by Granado *et al.* [63], a spin-phonon term $\omega_{\text{s-ph}} \propto \langle S_i \cdot S_j \rangle$ was added, where $\langle S_i \cdot S_j \rangle$ is the spin correlation function.
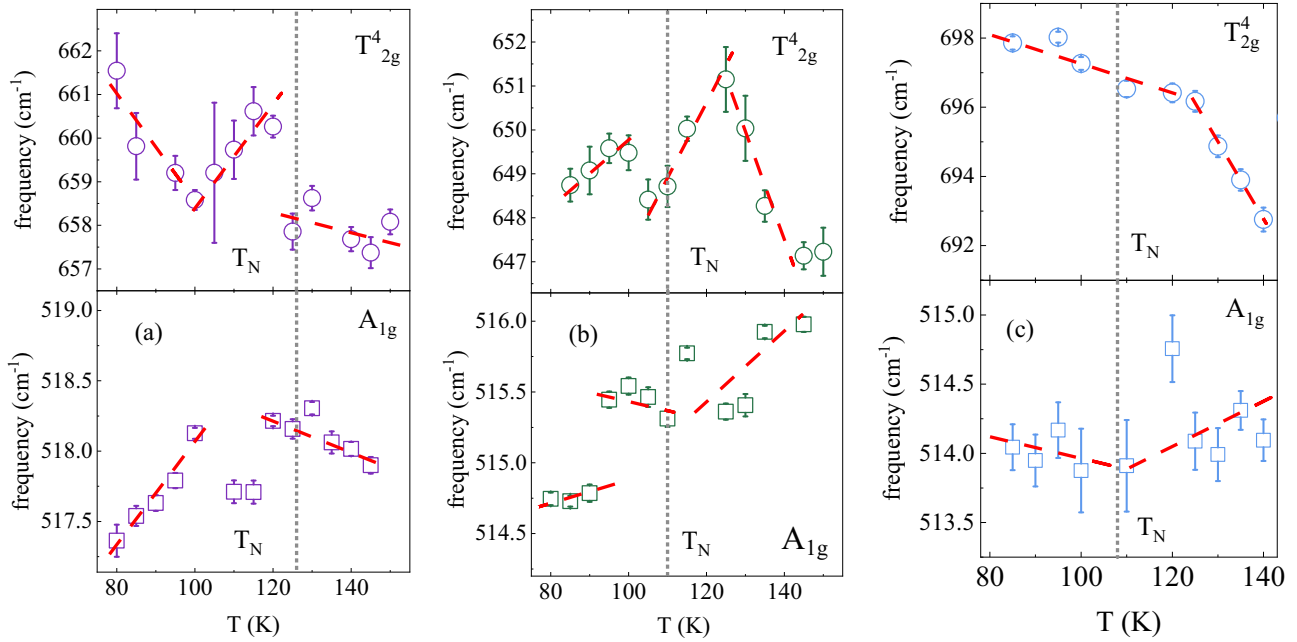
FIG. 7. Temperature-dependent frequency of T_{2g}^4 (top) and A_{1g} (bottom) Raman modes: (a) DIO, (b) DGIO, and (c) GIO. Red lines are guides to the eye. Gray dashed lines represent the magnetic ordering temperature.

So when the spin-spin correlation begins to show near the magnetic ordering temperature, the finite term $\omega_{s\text{-ph}}$ dominates, and one expects a deviation from the Balkanski model. It is, indeed, observed in our samples (Fig. S8 [33]). Strong spin-orbit coupling in pyrochlore iridates plays a role in spin exchange coupling and manifests as spin-phonon coupling near the magnetic ordering temperature T_N. Spin-phonon coupling can be a direct coupling or a combined one along with the magnetostriction. This can give rise to anomalous behavior in the phonon frequency through modification of the unit cell [27]. There is evidence of magnetostriction in the DIO sample in temperature-dependent magnetic irreversible data. We examine the hypothesis that the anomaly in the Raman mode frequencies, without a structural phase transition, is caused by direct spin-phonon coupling and the magnetostriction effect [64] using the FWHM of Raman modes near T_N. The FWHM is related to the phonon lifetime, and it is not affected by magnetostriction [65]. Figures 8 and 9 give the FWHM for the T_{2g}^4 [Ir-O(1) stretching vibrations] and A_{1g} [Ir-O(1)-Ir

bending vibrations] modes in DIO, DGIO, and GIO samples, respectively. It is clear that the FWHM of both Raman modes remains constant near the magnetic ordering temperature for the DIO sample, confirming the presence of magnetostriction in DIO. The increase in FWHM near T_N is consistent with direct spin-phonon coupling and the absence of magnetostriction in DGIO and GIO. In brief, there are anomalies in Raman mode frequencies near the magnetic transition temperature T_N for Dy- and Gd-based pyrochlore iridates. The deviation from the Balkanski model in A_{1g} and T_{2g}^4 modes near T_N indicates the presence of spin-phonon coupling. Its mediation by the magnetostriction effect in the DIO sample is confirmed because the FWHM remains constant near T_N. While the anomalies in the phonon frequency and increase in the FWHM near the magnetic transition for DGIO and GIO samples indicate direct spin-phonon coupling, the absence of magnetostriction in these substituted samples further supports this observation. Deviations of phonon frequency from the anharmonic model subside in the GIO sample. We believe
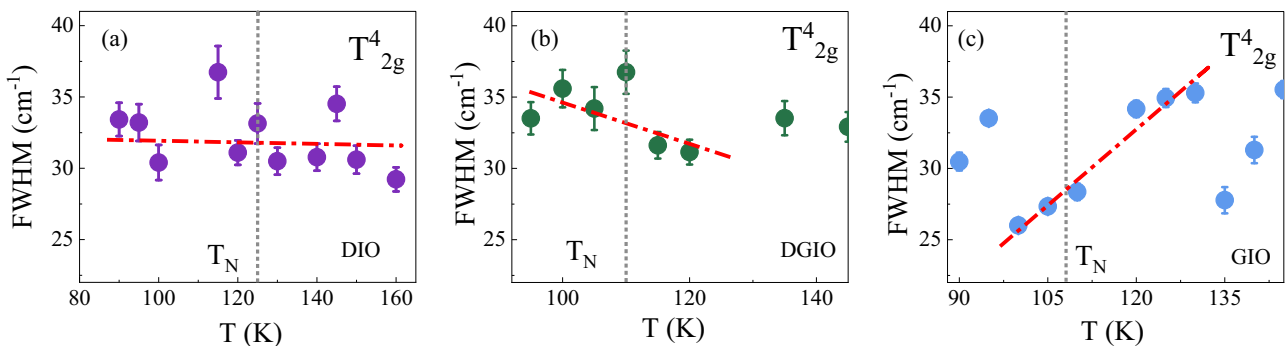

FIG. 8. Temperature dependence of FWHM for the T_{2g}^4 stretching mode for (a) DIO, (b) DGIO, and (c) GIO. The gray dashed lines indicate the temperatures where the magnetic ordering is observed, while the red dashed lines are guides to the eye.
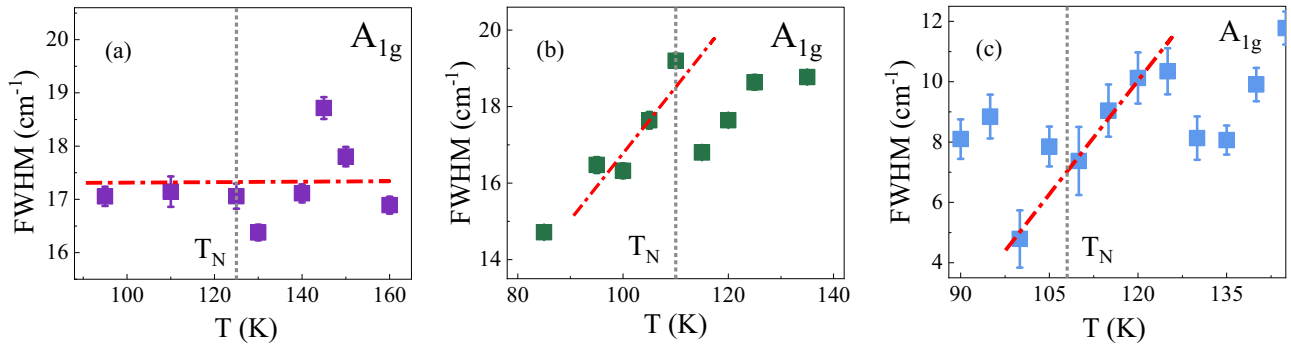
FIG. 9. Temperature dependence of FWHM for the A_{1g} bending mode in (a) DIO, (b) DGIO, and (c) GIO. The gray dashed lines indicate the temperatures where the magnetic ordering is observed, while the red dashed lines are a guide for the eye.

that the decrease in the f-d exchange interaction through the dilution of magnetic moment in the R site reduces the strength of spin-phonon coupling in GIO.

F. Temperature-dependent XRD

We use the temperature-dependent PXRD data to study the effect of the magnetostriction on the lattice constant near the ordering temperature T_N. Figures 10(a) and 10(b) give the lattice constant a'' obtained from the Rietveld refinements at different temperatures. Figures S9(a) and S9(b) in the Supplemental Material [33] show the refinement details. Figure 10(a) demonstrates changes in the lattice constant a'' below the Ir ordering temperature T_N for the DIO sample, and for the GIO sample, the lattice constant continues to decrease with temperature [Fig. 10(b)]. We applied linear fitting of a'' in two temperature regions: one above T_N and one below T_N for DIO [inset in Fig. 10(a)]. It shows a distinct deviation between two fittings near the Ir ordering temperature. This confirms the presence of magnetostriction in DIO. The decrease in lattice constant a'' arising from the decrease in the temperature is significantly reduced due to the expansion of a'' by magnetostriction. In Fig. 10(b), we fit the temperature-dependent lattice constant data for GIO for the entire temperature range (inset). There are no notable changes near T_N. This means that because the magnetic moment at the R site is small, the spin-phonon coupling strength is also small, and the magnetostriction is absent in the GIO sample. Hence, the temperature-dependent lattice constant continues to change in the same manner throughout without any significant change near or below T_N.

IV. CONCLUSION

In this work on the structural, electrical, and magnetic properties of $Dy_2Ir_2O_7$ (DIO), $(Dy_{0.5}Gd_{0.5})_2Ir_2O_7$ (DGIO), and $Gd_2Ir_2O_7$ (GIO), we presented the effect of partial and complete substitution of Dy^{3+} with Gd^{3+}. As Gd^{3+} has a higher ionic radius than Dy^{3+}, any increase in the Ir-O(1) bond length and decrease in the $\langle$Ir-O(1)-Ir$\rangle$ bond angle become crucial in determining the trigonal distortion in the $IrO(1)_6$ octahedra. Gd^{3+} substitution increases the trigonal distortion in the pyrochlore structure and influences the trigonal crystal field, spin-orbit coupling, and splitting of t_{2g} states. It effectively serves as a tool to tune the electric and mag-

netic properties. The three samples showed semiconducting behavior at high temperatures but shifted to a Mott insulating phase below T_{MIT}. Our findings show that T_{MIT} decreases with
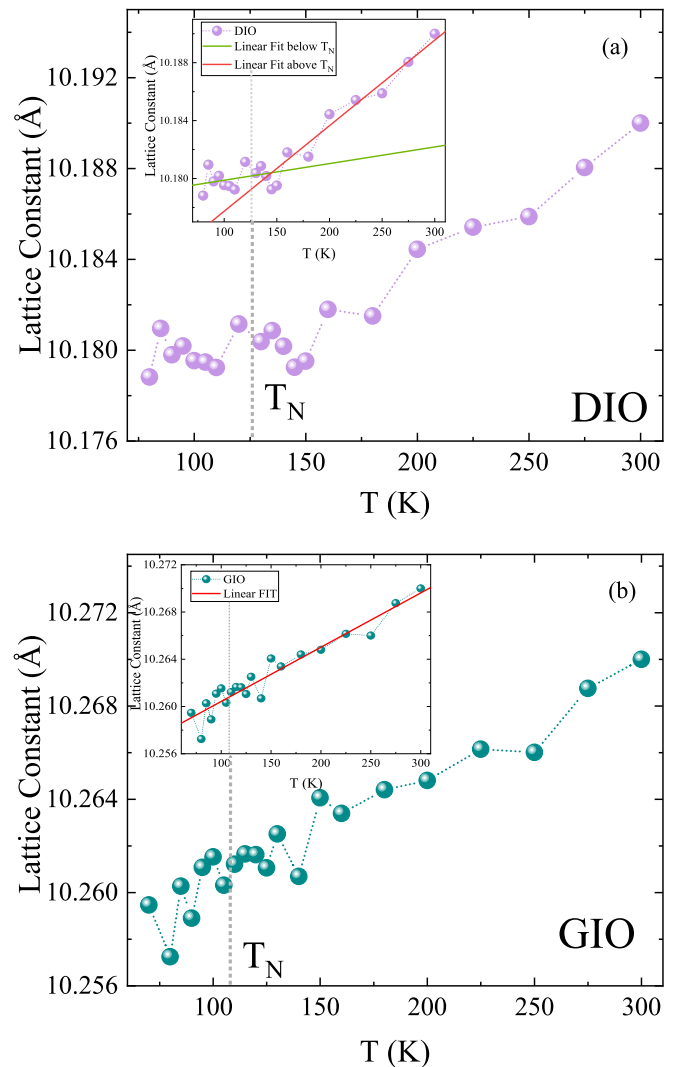

FIG. 10. Temperature dependence of lattice constant a'' in (a) DIO and (b) GIO samples. Gray dashed lines indicate respective magnetic ordering temperatures T_N in the DIO and GIO samples. The inset in (a) shows the linear fitting of a'' below (green line) and above (red line) T_N. The inset in (b) presents linear fitting (red line) in the whole temperature range.

Gd^{3+} substitution. Evidence of Ir^{4+} ordering (T_N) was seen at 126, 110, and 108 K in the DIO, DGIO, and GIO samples, respectively.

From the magnetization data, we observed the ordering of Ir^{4+} tetrahedra in a noncollinear AIAO structure near 100 K. This generates spin-phonon coupling in all three samples. In DIO, M_{irr} is negative at a low magnetic field ($\mu_0 H = 0.01$, 0.05, 0.1, and 0.5 T) but turns positive when $\mu_0 H = 1$T for the entire temperature range studied. For DGIO and GIO, M_{irr} values remain positive at all values of magnetic fields. The anomalies in the DIO sample are due to the presence of magnetostriction.

Raman spectroscopy measurements provide conclusive evidence of spin-phonon coupling in the form of anomalies in the A_{1g} and T_{2g}^4 modes in polycrystalline samples for DIO, DGIO, and GIO. For GIO, there were fewer anomalies. On lowering the temperature further, the f-d exchange interaction increases and tries to order the R-site tetrahedra. Due to the inherent higher moment of Dy^{3+}, ordered Dy^{3+} tetrahedra couple with the lattice and generate the magnetostriction in the DIO sample in addition to spin-phonon coupling. The FWHM for the T_{2g}^4 stretching mode and A_{1g} bending mode is almost constant for different temperatures in the DIO sample near T_N, whereas in DGIO and GIO, its magnitude changes markedly with temperature. The behavior of the FWHM near T_N supports the dominance of magnetostriction in the DIO sample while indicating the presence of only spin-phonon coupling and the absence of magnetostriction in the DGIO and GIO samples. We note from the susceptibility data that, by substituting Gd^{3+}, we can reduce the f-d exchange interaction and magnetostriction in the substituted compounds. The temperature dependence of the lattice constant of DIO showed a clear deviation near T_N, in agreement with magnetostriction. However, no significant changes were observed near T_N in the case of GIO, highlighting the absence of magnetostriction.

[1] J. E. Greedan, Geometrically frustrated magnetic materials, J. Mater. Chem. **11**, 37 (2001).

[2] R. Moessner and J. T. Chalker, Low-temperature properties of classical geometrically frustrated antiferromagnets, Phys. Rev. B **58**, 12049 (1998).

[3] J. E. Greedan, Frustrated rare earth magnetism: Spin glasses, spin liquids and spin ices in pyrochlore oxides, J. Alloys Compd. **408–412**, 444 (2006).

[4] H. R. Molavian, M. J. P. Gingras, and B. Canals, Dynamically induced frustration as a route to a quantum spin ice state in $Tb_2Ti_2O_7$ via virtual crystal field excitations and quantum many-body effects, Phys. Rev. Lett. **98**, 157204 (2007).

[5] J. S. Gardner, M. J. P. Gingras, and J. E. Greedan, Magnetic pyrochlore oxides, Rev. Mod. Phys. **82**, 53 (2010).

[6] C. R. Wiebe and A. M. Hallas, Frustration under pressure: Exotic magnetism in new pyrochlore oxides, APL Mater. **3**, 041519 (2015).

[7] D. Pesin and L. Balents, Mott physics and band topology in materials with strong spin–orbit interaction, Nat. Phys. **6**, 376 (2010).

[8] X. Wan, A. M. Turner, A. Vishwanath, and S. Y. Savrasov, Topological semimetal and Fermi-arc surface states in the electronic structure of pyrochlore iridates, Phys. Rev. B **83**, 205101 (2011).

[9] H. Shinaoka, Y. Motome, T. Miyake, S. Ishibashi, and P. Werner, First-principles studies of spin-orbital physics in pyrochlore oxides, J. Phys.: Condens. Matter **31**, 323001 (2019).

[10] A. B. Sushkov, J. B. Hofmann, G. S. Jenkins, J. Ishikawa, S. Nakatsuji, S. Das Sarma, and H. D. Drew, Optical evidence for a Weyl semimetal state in pyrochlore $Eu_2Ir_2O_7$, Phys. Rev. B **92**, 241108(R) (2015).

[11] D. Yanagishima and Y. Maeno, Metal-nonmetal changeover in pyrochlore iridates, J. Phys. Soc. Jpn. **70**, 2880 (2001).

[12] K. Matsuhira, M. Wakeshima, Y. Hinatsu, and S. Takagi, Metal-insulator transitions in pyrochlore oxides $Ln_2Ir_2O_7$, J. Phys. Soc. Jpn. **80**, 094701 (2011).

[13] S. M. Disseler, C. Dhital, A. Amato, S. R. Giblin, C. de la Cruz, S. D. Wilson, and M. J. Graf, Magnetic order in the pyrochlore iridates $A_2Ir_2O_7$ (A = Y, Yb), Phys. Rev. B **86**, 014428 (2012).

[14] H. Sagayama, D. Uematsu, T. Arima, K. Sugimoto, J. J. Ishikawa, E. O'Farrell, and S. Nakatsuji, Determination of long-range all-in-all-out ordering of Ir^{4+} moments in a pyrochlore iridate $Eu_2Ir_2O_7$ by resonant x-ray diffraction, Phys. Rev. B **87**, 100403(R) (2013).

[15] S. M. Disseler, Direct evidence for the all-in/all-out magnetic structure in the pyrochlore iridates from muon spin relaxation, Phys. Rev. B **89**, 140413(R) (2014).

[16] E. Lefrançois, V. Simonet, R. Ballou, E. Lhotel, A. Hadj-Azzem, S. Kodjikian, P. Lejay, P. Manuel, D. Khalyavin, and L. C. Chapon, Anisotropy-tuned magnetic order in pyrochlore iridates, Phys. Rev. Lett. **114**, 247202 (2015).

[17] S. Nakatsuji, Y. Machida, Y. Maeno, T. Tayama, T. Sakakibara, J. van Duijn, L. Balicas, J. N. Millican, R. T. Macaluso, and J. Y. Chan, Metallic spin-liquid behavior of the geometrically frustrated Kondo lattice $Pr_2Ir_2O_7$, Phys. Rev. Lett. **96**, 087204 (2006).

[18] Y. Machida, S. Nakatsuji, Y. Maeno, T. Tayama, and T. Sakakibara, Geometrical frustration and spin-liquid behavior of the metallic pyrochlore antiferromagnet $Pr_2Ir_2O_7$, J. Magn. Magn. Mater. **310**, 1328 (2007).

[19] J. Son, B. C. Park, C. H. Kim, H. Cho, S. Y. Kim, L. J. Sandilands, C. Sohn, J.-G. Park, S. J. Moon, and T. W. Noh, Unconventional spin-phonon coupling via the Dzyaloshinskii–Moriya interaction, npj Quantum Mater. **4**, 17 (2019).

[20] X. Moya and N. D. Mathur, Thermal Hall effect: Turn your phonon, Nat. Mater. **16**, 784 (2017).

[21] X. Zhang, Y. Zhang, S. Okamoto, and D. Xiao, Thermal Hall effect induced by magnon-phonon interactions, Phys. Rev. Lett. **123**, 167202 (2019).

[22] C. Calero, E. M. Chudnovsky, and D. A. Garanin, Field dependence of the electron spin relaxation in quantum dots, Phys. Rev. Lett. **95**, 166603 (2005).

[23] R. Ramesh and N. A. Spaldin, Multiferroics: Progress and prospects in thin films, Nat. Mater. **6**, 21 (2007).

[24] K. Ueda, R. Kaneko, A. Subedi, M. Minola, B. J. Kim, J. Fujioka, Y. Tokura, and B. Keimer, Phonon anomalies in pyrochlore iridates studied by Raman spectroscopy, Phys. Rev. B **100**, 115157 (2019).

[25] H. Kumar, V. G. Sathe, and A. K. Pramanik, Spin-phonon coupling in hole-doped pyrochlore iridates $Y_2(Ir_{1-x}Ru_x)_2O_7$: A Raman scattering study, J. Magn. Magn. Mater. **478**, 148 (2019).

[26] A. Thomas, P. Telang, K. Mishra, M. Cesnek, J. Bednarcik, D. V. S. Muthu, S. Singh, and A. K. Sood, Role of spin-phonon and electron-phonon interactions in the phonon renormalization of $(Eu_{1-x}Bi_x)_2Ir_2O_7$ across the metal-insulator phase transition: Temperature-dependent Raman and x-ray studies, Phys. Rev. B **105**, 075145 (2022).

[27] A. Nonato, B. S. Araujo, A. P. Ayala, A. P. Maciel, S. Yanez-Vilar, M. Sanchez-Andujar, M. Senaris-Rodriguez, and C. W. A. Paschoal, Spin-phonon and magnetostriction phenomena in $CaMn_7O_{12}$ helimagnet probed by Raman spectroscopy, Appl. Phys. Lett. **105**, 222902 (2014).

[28] Y. Feng, J. Bian, S. Chen, B. Fang, W. Tong, and H. Liu, Effects of Dy doping on the electrical transport and magnetic properties of the pyrochlore iridate $Bi_2Ir_2O_7$, J. Supercond. Novel Magn. **32**, 3979 (2019).

[29] S. Blundell, *Magnetism in Condensed Matter* (Oxford University Press, Oxford, 2001).

[30] R. Young, A. Sakthivel, T. Moss, and C. Paiva-Santos, *User's Guide to Program dbws-9411* (Georgia Institute of Technology, Atlanta, 1994).

[31] K. Momma and F. Izumi, Vesta: A three-dimensional visualization system for electronic and structural analysis, J. Appl. Crystallogr. **41**, 653 (2008).

[32] N. Fairley and C. S. Ltd., CasaXPS 2.3.15: CasaXPS processing software for XPS spectra (2009), http://www.casaxps.com.

[33] See Supplemental Material at http://link.aps.org/supplemental/10.1103/PhysRevB.108.134426 for XRD data along with Rietveld refinement, Ir 4f XPS spectra with fitting for different oxidation states, normalized resistivity data in both cooling and heating cycles, the first-order derivative of resistivity and magnetization data (Figs. S4 and S5, respectively), temperature-dependent ZFC and FCW data for the DIO sample at magnetic fields $\mu_0H = 0.01$ and 0.05 T in Fig. S6, Raman spectra along with the fitting at various temperatures, fitting of Raman modes T_{2g}^4 and A_{1g} with Balkanski's model in Fig. S8, and XRD data for the DIO and GIO samples at lower temperatures.

[34] W. Witczak-Krempa, G. Chen, Y. B. Kim, and L. Balents, Correlated quantum phenomena in the strong spin-orbit regime, Annu. Rev. Condens. Matter Phys. **5**, 57 (2014).

[35] B.-J. Yang and Y. B. Kim, Topological insulators and metal-insulator transition in the pyrochlore iridates, Phys. Rev. B **82**, 085111 (2010).

[36] H. Kumar, K. C. Kharkwal, K. Kumar, K. Asokan, A. Banerjee, and A. K. Pramanik, Magnetic and transport properties of the pyrochlore iridates $(Y_{1-x}Pr_x)_2Ir_2O_7$: Role of f-d exchange interaction and d-p orbital hybridization, Phys. Rev. B **101**, 064405 (2020).

[37] J. Flynn, J. Li, A. P. Ramirez, and M. Subramanian, The effect of iridium oxidation state on the electronic properties of perovskite-type solid solutions: $Ba_{2-x}La_xInIrO_6$ and $BaLaIn_{1-y}Ca_yIrO_6$, J. Solid State Chem. **247**, 53 (2017).

[38] H. Kumar, R. S. Dhaka, and A. K. Pramanik, Evolution of structure, magnetism, and electronic transport in the doped pyrochlore iridate $Y_2Ir_{2-x}Ru_xO_7$, Phys. Rev. B **95**, 054415 (2017).

[39] W. K. Zhu, M. Wang, B. Seradjeh, F. Yang, and S. X. Zhang, Enhanced weak ferromagnetism and conductivity in hole-doped pyrochlore iridate $Y_2Ir_2O_7$, Phys. Rev. B **90**, 054419 (2014).

[40] W. Yang, Y. Xie, W. Zhu, K. Park, A. Chen, Y. Losovyj, Z. Li, H. Liu, M. Starr, J. A. Acosta *et al.*, Epitaxial thin films of pyrochlore iridate $Bi_{2+x}Ir_{2-y}O_{7-\delta}$: Structure, defects and transport properties, Sci. Rep. **7**, 7740 (2017).

[41] H.-J. Koo, M.-H. Whangbo, and B. J. Kennedy, Similarities and differences in the structural and electronic properties of ruthenium and iridium pyrochlores $A_2M_2O_{7-y}$ (M= Ru, Ir), J. Solid State Chem. **136**, 269 (1998).

[42] S. Mondal, M. Modak, B. Maji, M. K. Ray, S. Mandal, S. K. Mandal, M. Sardar, and S. Banerjee, Role of f-d exchange interaction and Kondo scattering in the Nd-doped pyrochlore iridate $(Eu_{1-x}Nd_x)_2Ir_2O_7$, Phys. Rev. B **102**, 155139 (2020).

[43] N. F. Mott and E. A. Davis, *Electronic Processes in Non-crystalline Materials* (Oxford University Press, Oxford, 2012).

[44] B. I. Shklovskii and A. L. Efros, Variable-range hopping conduction, in *Electronic Properties of Doped Semiconductors* (Springer, Berlin, 1984), pp. 202–227.

[45] H. Liu, J. Bian, S. Chen, Y. Wang, Y. Feng, W. Tong, Y. Xie, and B. Fang, Enhanced ferromagnetism and Mott variable-range hopping behavior in Cu doped pyrochlore iridate $Y_2Ir_2O_7$, Phys. B (Amsterdam, Neth.) **568**, 60 (2019).

[46] H. Liu, D. Liang, S. Chen, J. Bian, Y. Feng, and B. Fang, Evolution of magnetic and transport properties in pyrochlore iridates $A_2Ir_2O_7$ (A= Y, Eu, Bi), Wuhan Univ. J. Nat. Sci. **22**, 215 (2017).

[47] M. C. Shapiro, S. C. Riggs, M. B. Stone, C. R. de la Cruz, S. Chi, A. A. Podlesnyak, and I. R. Fisher, Structure and magnetic properties of the pyrochlore iridate $Y_2Ir_2O_7$, Phys. Rev. B **85**, 214434 (2012).

[48] E. Lefrançois, L. Mangin-Thro, E. Lhotel, J. Robert, S. Petit, V. Cathelin, H. E. Fischer, C. V. Colin, F. Damay, J. Ollivier, P. Lejay, L. C. Chapon, V. Simonet, and R. Ballou, Spin decoupling under a staggered field in the $Gd_2Ir_2O_7$ pyrochlore, Phys. Rev. B **99**, 060401(R) (2019).

[49] V. Cathelin, E. Lefrançois, J. Robert, P. C. Guruciaga, C. Paulsen, D. Prabhakaran, P. Lejay, F. Damay, J. Ollivier, B. Fåk, L. C. Chapon, R. Ballou, V. Simonet, P. C. W. Holdsworth, and E. Lhotel, Fragmented monopole crystal, dimer entropy, and Coulomb interactions in $Dy_2Ir_2O_7$, Phys. Rev. Res. **2**, 032073(R) (2020).

[50] S. M. Disseler, C. Dhital, T. C. Hogan, A. Amato, S. R. Giblin, C. de la Cruz, A. Daoud-Aladine, S. D. Wilson, and M. J. Graf, Magnetic order and the electronic ground state in the pyrochlore iridate $Nd_2Ir_2O_7$, Phys. Rev. B **85**, 174441 (2012).

[51] G. Chen and M. Hermele, Magnetic orders and topological phases from f-d exchange in pyrochlore iridates, Phys. Rev. B **86**, 235129 (2012).

[52] B. C. Zhao, Y. Q. Ma, W. H. Song, and Y. P. Sun, Magnetization steps in the phase separated manganite $La_{0.275}Pr_{0.35}Ca_{0.375}MnO_3$, Phys. Lett. A **354**, 472 (2006).

[53] F. J. Darnell, Magnetostriction in dysprosium and terbium, Phys. Rev. **132**, 128 (1963).

[54] T. Hasegawa, N. Ogita, K. Matsuhira, S. Takagi, M. Wakeshima, Y. Hinatsu, and M. Udagawa, Raman scattering study in iridium pyrochlore oxides, J. Phys.: Conf. Ser. **200**, 012054 (2010).

[55] K. Taniguchi, T. Katsufuji, S. Iguchi, Y. Taguchi, H. Takagi, and Y. Tokura, Raman study of the metal-insulator transition in pyrochlore Mo oxides, Phys. Rev. B **70**, 100401(R) (2004).

[56] B. Mihailova, S. Stoyanov, V. Gaydarov, M. Gospodinov, and L. Konstantinov, Raman spectroscopy study of pyrochlore $Pb_2Sc_{0.5}Ta_{1.5}O_{6.5}$ crystals, Solid State Commun. **103**, 623 (1997).

[57] M. Mączka, J. Hanuza, K. Hermanowicz, A. Fuentes, K. Matsuhira, and Z. Hiroi, Temperature-dependent Raman scattering studies of the geometrically frustrated pyrochlores $Dy_2Ti_2O_7$, $Gd_2Ti_2O_7$ and $Er_2Ti_2O_7$, J. Raman Spectrosc. **39**, 537 (2008).

[58] E. Granado, P. G. Pagliuso, J. A. Sanjurjo, C. Rettori, M. A. Subramanian, S.-W. Cheong, and S. B. Oseroff, Phonon Raman scattering in $A_2Mn_2O_7$ (A = Tl, In, Y), Phys. Rev. B **60**, 6513 (1999).

[59] M. Das, S. Bhowal, J. Sannigrahi, A. Bandyopadhyay, A. Banerjee, G. Cibin, D. Khalyavin, N. Banerjee, D. Adroja, I. Dasgupta, and S. Majumdar, Interplay between structural, magnetic, and electronic states in the pyrochlore iridate $Eu_2Ir_2O_7$, Phys. Rev. B **105**, 134421 (2022).

[60] H. Kumar and A. K. Pramanik, Nonequilibrium low temperature phase in pyrochlore iridate $Y_2Ir_2O_7$: Possibility of glass-like dynamics, J. Magn. Magn. Mater. **409**, 20 (2016).

[61] E. Cazzanelli, A. Kuzmin, G. Mariotto, and N. Mironova-Ulmane, Study of vibrational and magnetic excitations in $Ni_cMg_{1-c}O$ solid solutions by Raman spectroscopy, J. Phys.: Condens. Matter **15**, 2045 (2003).

[62] M. Balkanski, R. F. Wallis, and E. Haro, Anharmonic effects in light scattering due to optical phonons in silicon, Phys. Rev. B **28**, 1928 (1983).

[63] E. Granado, A. García, J. A. Sanjurjo, C. Rettori, I. Torriani, F. Prado, R. D. Sánchez, A. Caneiro, and S. B. Oseroff, Magnetic ordering effects in the Raman spectra of $La_{1-x}Mn_{1-x}O_3$, Phys. Rev. B **60**, 11879 (1999).

[64] H.-M. Eiter, P. Jaschke, R. Hackl, A. Bauer, M. Gangl, and C. Pfleiderer, Raman study of the temperature and magnetic-field dependence of the electronic and lattice properties of MnSi, Phys. Rev. B **90**, 024411 (2014).

[65] V. S. Bhadram, B. Rajeswaran, A. Sundaresan, and C. Narayana, Spin-phonon coupling in multiferroic $RCrO_3$ (Ry, Lu, Gd, Eu, Sm): A Raman study, Europhys. Lett. **101**, 17008 (2013).